PERGAMON

International Journal of Heat and Mass Transfer 45 (2002) 2587–2595

International Journal of HEAT and MASS TRANSFER

www.elsevier.com/locate/ijhmt

Forced convection in a wavy-wall channel

C.-C. Wang, C.-K. Chen *

Department of Mechanical Engineering, National Cheng-Kung University, Tainan, Taiwan 701 People's Republic of China

Received 27 December 2000; received in revised form 29 August 2001

Abstract

The rates of heat transfer for flow through a sinusoidally curved converging–diverging channel has been analyzed using a simple coordinate transformation method and the spline alternating-direction implicit method. The effects of the wavy geometry, Reynolds number and Prandtl number on the skin-friction and Nusselt number have been studied. Results show that the amplitudes of the Nusselt number and the skin-friction coefficient increase with an increase in the Reynolds number and the amplitude–wavelength ratio. The heat transfer enhancement is not significant at smaller amplitude wavelength ratio, however, at a sufficiently larger value of amplitude wavelength ratio the corrugated channel will be seen to be an effective heat transfer device, especially at higher Reynolds numbers. © 2002 Published by Elsevier Science Ltd.

Keywords: Forced convection; Wavy-wall channel; Cubic spline

1. Introduction

The corrugated wall channel is one of several devices employed for enhancing the heat transfer efficiency of industrial transport processes. The problem of viscous flow in wavy channels was first treated analytically by Burns and Parks [1], who expressed the stream function as a Fourier series under the assumption of Stokes flow. Following this, Goldstein and Sparrow [2] were the first to use the naphthalene technique to measure local and average heat transfer coefficients in a corrugated wall channel (with 'triangular waves'). Their experiments in laminar, transitional and turbulent flows used two corrugation cycles (i.e. two wavelengths). They observed secondary flows in the regions of high resolution local mass transfer measurement, and comparison of their results with those obtained with parallel-plate channels showed a threefold enhancement in the average heat transfer in the turbulent regimes. However, there was an even greater penalty in the pumping power required. In order to avoid the entrance effect, O'Brien and Sparrow [3] performed a complete study on the same geometry with more corrugation cycles. Result shows that a heat transfer enhancement by a factor of about 2.5 over a conventional straight channel was observed in fully developed region.

In 1993, Saniei and Dini [4] experimentally study heat transfer characteristics in the turbulent regime for a wavy-wall channel. They found that the maximum local Nusselt number was located upstream of the peak of each wave, while the minimum local Nusselt number was located downstream, within a short distance of the peak of each wave. They determined that the highest average Nusselt number belongs to the second wave and that the Nusselt number remains constant downstream of the third wave as a result of the flow being fully developed periodically. In recent numerical simulations, Wang and Vanka [5] determined the rates of heat transfer for a flow through a periodic array of wavy passages. They observed that in the steady-flow regime, the average Nusselt numbers for the wavy-wall channel were only slightly larger than those for a parallel-plate channel. However, in the transitional-flow regime, the enhancement of heat transfer was by a factor of approximately 2.5. Friction factors for the wavy channel were about twice those for the parallel-plate channel in the steady-flow region, and remained almost constant in the transitional regime. More recently, the experimental study of flows and heat transfer in sinusoidal wavy passages was conducted by

* Corresponding author. Tel.: +886-6-275-7575; fax: +886-6-234-2081.

E-mail address: ckchen@mail.ncku.edu.tw (C.-K. Chen).

0017-9310/02/$ - see front matter © 2002 Published by Elsevier Science Ltd.
PII: S0017-9310(01)00335-0

Nomenclature

a	amplitude of wavy surface
C_f	skin-friction coefficient
C_p	specific heat of fluid at constant pressure
h	heat transfer coefficient
K_f	thermal conductivity
L	half separation distance between wavy walls
$Nu_{\bar{x}}, Nu_m$	local Nusselt number and average Nusselt number, respectively
Pr	Prandtl number
Re	generalized Reynolds number
S	surface geometry function
T	temperature
u, v	x and y velocity components, respectively
U_m	average velocity
x, y	axial and transverse (Cartesian) coordinates, respectively

Greek symbols

α	wavy amplitude–wavelength ratio
μ	dynamic viscosity
θ	dimensionless temperature
ρ	density of fluid
σ	distance measured along surface from wavy wall
τ_w	skin-friction
ω	vorticity
ξ, η	transformed coordinates
ψ	stream function

Superscripts

–	dimensional quantity
′	derivative with respect to x

Subscripts

e	end point of wavy wall
m	mean value
s	start point of wavy wall
w	surface conditions
x	local value

Rush et al. [6]. Using visualization methods, the flow field was characterized as steady or unsteady, with special attention directed towards detecting the onset of macroscopic mixing in the flow. The location of the onset of mixing was found to depend upon the Reynolds number and the channel geometry.

Although some studies for steady and unsteady flows have been reported, e.g. [7–10], little knowledge is available on the flow in these wavy channels. The study presented in this paper employs a simple coordinate transformation method to transform a complex wavy channel into a parallel-plate channel. The equations obtained are then solved using the spline alternating-direction implicit (SADI) method. Since the SADI method can evaluate the spatial derivative terms directly without any finite difference discretization, the gradient boundary conditions may be represented more accurately, and irregular boundaries are easier to deal with. The effects of the Reynolds number, the Prandtl number and the dimensionless amplitude of the wavy surface on the skin-friction coefficient and Nusselt number have all been examined in this study.

2. Mathematical formulation

In this study, flow in a symmetric wavy-wall channel was analyzed, as shown in Fig. 1. The working fluid was assumed to be Newtonian fluid with constant fluid properties, and the flow was considered to be laminar, incompressible, steady and two-dimensional. Viscous dissipation was neglected, because it has a negligible effect

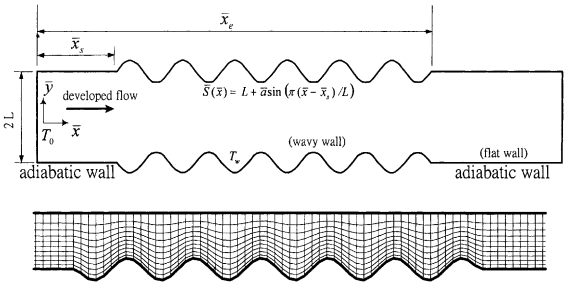

Fig. 1. Physical model, coordinates and grid system.

(see [11]). The above assumptions were designed to keep the theoretical model as simple as possible. For forced convection, the fluid and thermal fields are governed by the dimensionless equations of stream function, vorticity transport and energy. These may be written in the form

$$\nabla^2\psi = -\omega, \tag{1}$$

$$u\frac{\partial\omega}{\partial\bar{x}} + v\frac{\partial\omega}{\partial y} = \frac{1}{Re}\nabla^2\omega, \tag{2}$$

$$u\frac{\partial\theta}{\partial x} + v\frac{\partial\theta}{\partial y} = \frac{1}{Re\,Pr}\nabla^2\theta, \tag{3}$$

where

$$\omega = \frac{\partial v}{\partial x} - \frac{\partial u}{\partial y}, \quad u = \frac{\partial\psi}{\partial y}, \quad v = -\frac{\partial\psi}{\partial x},$$

$$\nabla^2 = \frac{\partial^2}{\partial x^2} + \frac{\partial^2}{\partial y^2} \tag{4}$$

and the dimensionless quantities are defined:

$$x=\frac{\bar{x}}{L},\quad y=\frac{\bar{y}}{L},\quad \alpha=\frac{\bar{a}}{L},\quad S(x)=\frac{\bar{S}(\bar{x})}{L},$$
$$u=\frac{\bar{u}}{U_{\mathrm{m}}},\quad v=\frac{\bar{v}}{U_{\mathrm{m}}},\quad \omega=\frac{\bar{\omega}L}{U_{\mathrm{m}}},\quad \psi=\frac{\bar{\psi}}{U_{\mathrm{m}}L},$$
$$\theta=\frac{T-T_0}{T_{\mathrm{w}}-T_0},\quad Re=\frac{\rho U_{\mathrm{m}}L}{\mu},\quad Pr=\frac{\mu C_{\mathrm{p}}}{K_{\mathrm{f}}}. \tag{5}$$

Note that U_{m} is the average mean velocity in the wavy channel. $\bar{u}$ and $\bar{v}$ are the components of the velocity in the $\bar{x}$ and $\bar{y}$ directions. ρ, μ and T are the density, viscosity and temperature of the fluid. K_{f} and C_{p} are the thermal conductivity and the specific heat of the fluid at constant pressure.

It is assumed that the axis of symmetry is aligned with the oncoming fully developed Poiseuille flow. As will be seen in Fig. 1, the shape of the low wavy-wall profile in the region $\bar{x}_{\mathrm{s}}\leqslant\bar{x}\leqslant\bar{x}_{\mathrm{e}}$ is given as

$$\bar{S}(\bar{x})=-L-\bar{a}\sin\left[\pi(\bar{x}-\bar{x}_{\mathrm{s}})/L\right], \tag{6}$$

where $\bar{x}_{\mathrm{s}}$ and $\bar{x}_{\mathrm{e}}$ are the start and end points of the wavy-wall channel, respectively, and $\bar{a}$ is the amplitude of the wavy surface. Furthermore, it is assumed that the temperature of the wavy surface is held at a constant value T_{w}, which is higher than the entrance fluid temperature T_0. Thus, the corresponding boundary conditions are considered as follows:

1. At the wavy surface $[y=-S(x)]$:

$$\psi=-1,\quad u=v=0, \tag{7}$$
$$\theta=1\quad \text{for } x_{\mathrm{s}}\leqslant x\leqslant x_{\mathrm{e}}, \tag{8}$$
$$\frac{\partial\theta}{\partial y}=0\quad \text{for } x<x_{\mathrm{s}} \text{ or } x\geqslant x_{\mathrm{e}}. \tag{9}$$

2. At the symmetric axis of channel ($y=0$):

$$\psi=\omega=0,\quad \frac{\partial\theta}{\partial y}=0. \tag{10}$$

3. At the inlet section ($x=0$):

$$\psi=\frac{3}{2}\left(y-\frac{y^3}{3}\right),\quad \omega=3y,\quad \theta=0. \tag{11}$$

4. At the outlet section ($x\to\infty$):

$$\frac{\partial\psi}{\partial x}=0,\quad \frac{\partial\omega}{\partial x}=0,\quad \frac{\partial\theta}{\partial x}=0. \tag{12}$$

In order to resolve the irregular boundary, we define new variables by eliminating the effect of the wavy surface. The transformed coordinates are

$$\xi=x,\quad \eta=\frac{y}{S(x)}. \tag{13}$$

Therefore, by substituting Eq. (13) into Eqs. (1)–(4), the governing equations are transformed a wavy-wall channel into a parallel-plate channel. The transformed equations are given as

$$\nabla^2\psi=-\omega, \tag{14}$$
$$u\left(\frac{\partial\omega}{\partial\xi}+\eta_x\frac{\partial\omega}{\partial\eta}\right)+v\eta_y\frac{\partial\omega}{\partial\eta}=\frac{1}{Re}\nabla^2\omega, \tag{15}$$
$$u\left(\frac{\partial\theta}{\partial\xi}+\eta_x\frac{\partial\theta}{\partial\eta}\right)+v\eta_y\frac{\partial\theta}{\partial\eta}=\frac{1}{RePr}\nabla^2\theta, \tag{16}$$

where

$$u=\eta_y\frac{\partial\psi}{\partial\eta},\quad v=-\left(\frac{\partial\psi}{\partial\xi}+\eta_x\frac{\partial\psi}{\partial\eta}\right),$$
$$\omega=\frac{\partial v}{\partial\xi}+\eta_x\frac{\partial v}{\partial\eta}-\eta_y\frac{\partial u}{\partial\eta},$$
$$\nabla^2=\frac{\partial^2}{\partial\xi^2}+\left(\eta_x^2+\eta_y^2\right)\frac{\partial^2}{\partial\eta^2}+2\eta_x\frac{\partial^2}{\partial\xi\,\partial\eta}+\left(\eta_{xx}+\eta_{yy}\right)\frac{\partial}{\partial\eta},$$
$$\eta_y=\frac{1}{S(x)},\quad \eta_x=\frac{-yS'(x)}{S^2(x)},$$
$$\eta_{xx}=\frac{y\left(2S'^2-SS''\right)}{S^3(x)},\quad \eta_{yy}=0. \tag{17}$$

The nonlinear elliptic equations (14)–(17) must be solved subject to the following boundary conditions:

(a) At the wavy surface ($\eta=-1$):

$$\psi=-1,\quad u=v=0, \tag{18}$$
$$\theta=1\quad \text{for } \xi_{\mathrm{s}}\leqslant\xi\leqslant\xi_{\mathrm{e}}, \tag{19}$$
$$\frac{\partial\theta}{\partial\eta}=0\quad \text{for } \xi<\xi_{\mathrm{s}} \text{ or } \xi\geqslant\xi_{\mathrm{e}}. \tag{20}$$

(b) At the symmetric axial of channel ($\eta=0$):

$$\psi=\omega=0,\quad \frac{\partial\theta}{\partial\eta}=0. \tag{21}$$

(c) At the inlet section ($\xi=0$):

$$\psi=\frac{3}{2}\left(\eta-\frac{\eta^3}{3}\right),\quad \omega=3\eta,\quad \theta=0. \tag{22}$$

(d) At the outlet section ($\xi\to\infty$):

$$\frac{\partial\psi}{\partial\xi}=0,\quad \frac{\partial\omega}{\partial\xi}=0,\quad \frac{\partial\theta}{\partial\xi}=0. \tag{23}$$

Once the flow and the temperature fields have been obtained, several important quantities can be calculated, as presented below.

The local Nusselt number at the surface of the wavy-wall channel is defined as:

$$Nu_{\bar{x}}=\frac{h_{\bar{x}}L}{K_{\mathrm{f}}}=\frac{-(\partial T/\partial n)L}{T_{\mathrm{w}}-T_0}, \tag{24}$$

where

$$\frac{\partial T}{\partial n} = \sqrt{\left(\frac{\partial T}{\partial \bar{x}}\right)^2 + \left(\frac{\partial T}{\partial \bar{y}}\right)^2} \tag{25}$$

and $\partial/\partial n$ represents the differentiation with respect to the coordinate normal to the surface. The axial distribution of Nu_x can be given as

$$Nu_x = \left(\eta_x^2 + \eta_y^2\right)^{1/2} \frac{\partial \theta}{\partial \eta}. \tag{26}$$

The average Nusselt number is defined as

$$Nu_m = \frac{h_m L}{K_f} \frac{\bar{\sigma}}{\bar{x}}. \tag{27}$$

It should be noted that the average Nusselt values are obtained by averaging the heat transfer over the surface from the start point of the wavy wall to $\sigma(x)$. Thus, the value of Nu_m may be calculated as

$$Nu_m = \frac{1}{\xi - \xi_s} \int_{\xi_s}^{\xi} \left(1 + S'^2\right)^{1/2} \left(\eta_x^2 + \eta_y^2\right)^{1/2} \frac{\partial \theta}{\partial \eta} \, d\xi, \tag{28}$$

where

$$h_m = \frac{q_m}{T_w - T_0}, \tag{29}$$

$$q_m = \frac{1}{\bar{\sigma}} \int_{x_s}^{\sigma} -K_f \frac{\partial T}{\partial n} \, d\bar{\sigma}, \tag{30}$$

$$\bar{\sigma} = \int_{x_s}^{x} \left(1 + \bar{S}'^2\right)^{1/2} d\bar{x}. \tag{31}$$

Finally, the shear force at the surface is

$$\tau_w = \mu \left(\frac{\partial \bar{u}}{\partial \bar{y}} + \frac{\partial \bar{v}}{\partial \bar{x}} \right)_{\bar{y}=\bar{S}(\bar{x})}. \tag{32}$$

And the skin-friction coefficient, C_f, may be defined as

$$C_f = \frac{\tau_w}{\rho U_m^2}. \tag{33}$$

Substitution of Eq. (32) into Eq. (33) yields

$$Re \; C_f = [\eta_y^2 - \eta_x^2] \frac{\partial^2 \psi}{\partial \eta^2}. \tag{34}$$

3. Numerical method

The dimensionless governing differential equations (14)–(16), combined with the relevant boundary conditions (18)–(23), are solved numerically using the spline alternating-direction implicit method [12,13]; an improved version of the cubic spline collocation method [14]. Using the false transient technique, Eqs. (14)–(16) may be transformed as

$$\frac{\psi_{i,j}^{n+1} - \psi_{i,j}^{n}}{\Delta \tau} + \nabla^2 \psi_{i,j} = -\omega_{i,j}^{n}, \tag{35}$$

$$\frac{\omega_{i,j}^{n+1} - \omega_{i,j}^{n}}{\Delta \tau} + u\left(l_w^{n+1} + \eta_x m_w^n\right) + v\eta_y m_w^n = \frac{1}{Re} \nabla^2 \omega_{i,j}, \tag{36}$$

$$\frac{\theta_{i,j}^{n+1} - \theta_{i,j}^{n}}{\Delta \tau} + u\left(l_\theta^{n+1} + \eta_x m_\theta^n\right) + v\eta_y m_\theta^n = \frac{1}{RePr} \nabla^2 \theta_{i,j}, \tag{37}$$

where

$$u = \eta_y m_\psi^n, \quad v = -\left(l_\psi^{n+1} + \eta_x m_\psi^n\right),$$

$$\nabla^2 = L_\phi^{n+1} + (\eta_x^2 + \eta_y^2) M_\phi^{n+1} + 2\eta_x \frac{(l_\phi)_{i,j+1}^n - (l_\phi)_{i,j-1}^n}{2\Delta \eta} + (\eta_{xx} + \eta_{yy}) m_\phi^n,$$

$$l_\phi = \frac{\partial \phi}{\partial \xi}, \quad L_\phi = \frac{\partial^2 \phi}{\partial \xi^2}, \quad m_\phi = \frac{\partial \phi}{\partial \eta}, \quad M_\phi = \frac{\partial^2 \phi}{\partial \eta^2} \tag{38}$$

and ϕ represents refers to ψ, ω or θ. $\Delta \tau = \tau^{n+1} - \tau^n$ represents the false time-step.

Using the spline alternating-direction implicit method, Eqs. (35)–(37) may be expressed as

$$\phi_{i,j}^{n+1} = F_{i,j} + G_{i,j} l_{i,j}^{n+1} + S_{i,j} L_{i,j}^{n+1}, \tag{39}$$

where i and j refer to the computational nodes and n is the false time-step. $F_{i,j}$, $G_{i,j}$ and $S_{i,j}$ are the known coefficients evaluated at the previous time-step, as shown in Table 1. Using cubic spline collocation relations [14], Eq. (39) may be expressed in tri-diagonal form

$$A_{i,j} \varphi_{i,j}^{n+1} + B_{i,j} \varphi_{i,j}^{n+1} + C_{i,j} \varphi_{i,j}^{n+1} = D_{i,j}, \tag{40}$$

where φ represents ψ, ω and θ, or its first or second derivatives. Equation (40) may be easily solved by the Thomas algorithm.

The numerical procedure is as follows:

1. Establish suitable boundary conditions;
2. Apply the spline alternating-direction implicit method to solve (35)–(37) to obtain ψ, ω and θ;
3. Return to step 1 to calculate the results for the next fictitious time-step. The solutions obtained are treated as steady-state solutions when the convergent criteria are satisfied, i.e.

$$\left| \frac{\varphi_{i,j}^{n+1} - \varphi_{i,j}^{n}}{\varphi_{i,j}^{n+1}} \right| < 1 \times 10^{-5}, \tag{41}$$

where n denotes the number of iterations.

4. When the steady state is reached, iteration is complete.

Table 1
Value of $F_{i,j}$, $G_{i,j}$, and $S_{i,j}$

ψ	$F_{i,j}$	$\psi_{i,j}^n - \Delta\tau\left[\omega_{i,j}^{n+1} + \left(\eta_x^2 + \eta_y^2\right)M_\psi^{n+1} + 2\eta_x\dfrac{(l_\psi)_{i,j+1}^n - (l_\psi)_{i,j-1}^n}{2\Delta\eta} + \left(\eta_{xx} + \eta_{yy}\right)m_\psi^n\right]$
	$G_{i,j}$	0
	$S_{i,j}$	$-\Delta\tau$
ω	$F_{i,j}$	$\omega_{i,j}^n + \Delta\tau\left[-\eta_y m_\psi^n \eta_x m_w^n + (l_\psi^{\eta+1} + \eta_x m_\psi^n)\eta_y m_w^n + \dfrac{1}{Re}\left(\left(\eta_x^2 + \eta_y^2\right)M_\omega^{n+1} + 2\eta_x\dfrac{(l_\omega)_{i,j+1}^n - (l_\omega)_{i,j-1}^n}{2\Delta\eta} + \left(\eta_{xx} + \eta_{yy}\right)m_\omega^n\right)\right]$
	$G_{i,j}$	$-\Delta\tau\eta_y m_\psi^n$
	$S_{i,j}$	$\Delta\tau\frac{1}{Re}$
θ	$F_{i,j}$	$\theta_{i,j}^n + \Delta\tau\left[-\eta_y m_\psi^n \eta_x m_\theta^n + (l_\psi^{n+1} + \eta_x m_\psi^n)\eta_y m_\theta^n + \dfrac{1}{RePr}\left(\left(\eta_x^2 + \eta_y^2\right)M_\theta^{n+1} + 2\eta_x\dfrac{(l_\theta)_{i,j+1}^n - (l_\theta)_{i,j-1}^n}{2\Delta\eta} + \left(\eta_{xx} + \eta_{yy}\right)m_\theta^n\right)\right]$
	$G_{i,j}$	$-\Delta\tau\eta_y m_\psi^n$
	$S_{i,j}$	$\Delta\tau(1/(RePr))$

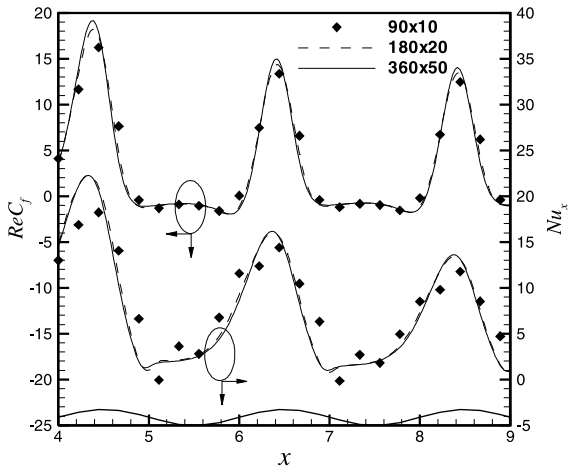

Fig. 2. Distribution of skin-friction coefficient and local Nusselt number for different grid sizes at $\alpha = 0.2$, $Re = 300$ and $Pr = 6.93$.

4. Results and discussion

Fig. 2 shows that an accuracy test of grid fineness is made for grids of 360×50, 180×20 and 90×10 at $Re = 300$, $\alpha = 0.2$ and $Pr = 6.93$, $\xi \in [0, 20]$ and $\eta \in [-1, 0]$. Comparing the grids of 90×10 and 360×50, it will be observed that although the skin-friction coefficients of the two grids match very closely, there are same discrepancies in the Nusselt numbers in the furrow of each wave. This indicates that more grids are required to resolve the temperature field, in order to gain a better result for the Nusselt number. As will be observed more clearly in Fig. 2, the results for grids of 180×20 in this study are in good agreement with those obtained by grids of 360×50 for the skin-friction coefficient and local Nusselt number. Thus, as shown in Fig. 1, a 180×20 nonuniform grid with smaller spacing mesh points in the neighborhood of the fluid–solid boundary at η-direction is used in this study. In addition, numerical experiments were carried out to ensure the independence of the results on the parallel-plate length of the inlet and outlet. The results were obtained for the lower surface described by $S(\xi) = -1 - \alpha\sin(\pi(\xi - 3))$ at $3 \leqslant \xi \leqslant 15$ (i.e. six complete sinusoidal waves) with different amplitude–wavelength ratios and Reynolds numbers. Two different values of Prandtl number $Pr = 6.93$ and 0.71 were also considered.

Figs. 3–6 show the distributions of the local skin-friction coefficient, streamlines, local Nusselt number and average Nusselt number for three values of wavy amplitude–wavelength ratios (i.e. $\alpha = 0, 0.1$ and 0.2) when $Re = 500$ and $Pr = 6.93$. Fig. 3 shows that since the entrance condition is fully developed flow, then, the local skin-friction coefficient is constant at all locations for a parallel-plate channel (i.e. $\alpha = 0$). In the case of wavy-wall channel, with a wavy amplitude–wavelength ratio, α, of 0.1, the harmonic curve for the local skin-friction coefficient in the region of wavy channel has the same frequency as that of the wavy surface, and the maximum and minimum values occur precisely at the locations of minimum and maximum cross-section of the wavy-wall channel. As will be seen more clearly in Fig. 4(a), since the flow reversal occurs between the separated point ($\xi = 5.1$) and the reattachment point

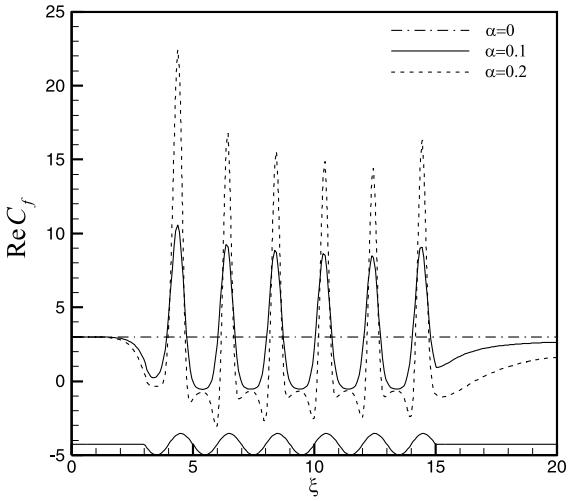

Fig. 3. Distribution of skin-friction coefficient for $Re = 500$ and $Pr = 6.93$.

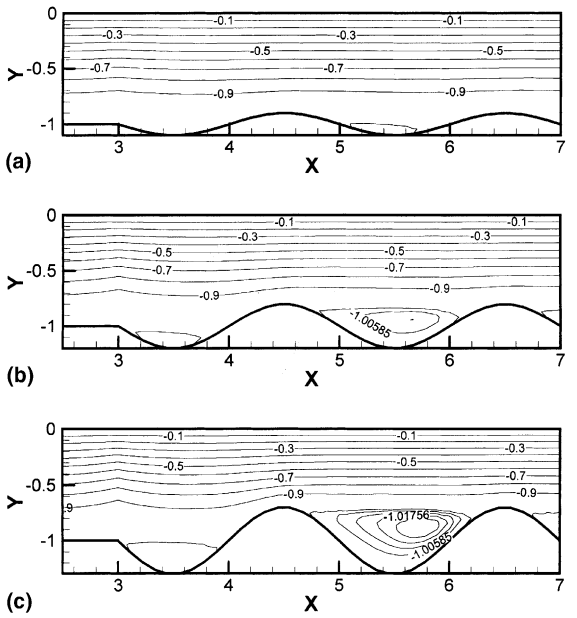

Fig. 4. Streamlines of flow for various amplitude–wavelength ratios at $Re = 500$ and $Pr = 6.93$: (a) $\psi_{\min} = -1.03059,\ \alpha = 0.1$; (b) $\psi_{\min} = -1.00046,\ \alpha = 0.2$; (c) $\psi_{\min} = -1.01195,\ \alpha = 0.3$.

($\xi = 5.67$), the skin-friction coefficient is negative in the furrow of the wavy-wall channel. In this paper, the locations of the separation and reattachment points are determined from the sign of the near wall vorticity. Moreover, as the wavy amplitude–wavelength ratio is increased to 0.2 and to 0.3, the distance of the separated and reattachment points also increases as shown in Figs. 4(a) and (b). It should be noted that the major region of

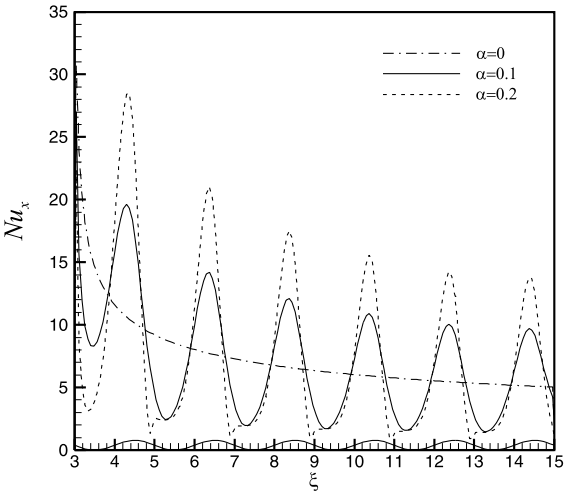

Fig. 5. Distribution of local Nusselt number for $Re = 500$ and $Pr = 6.93$.

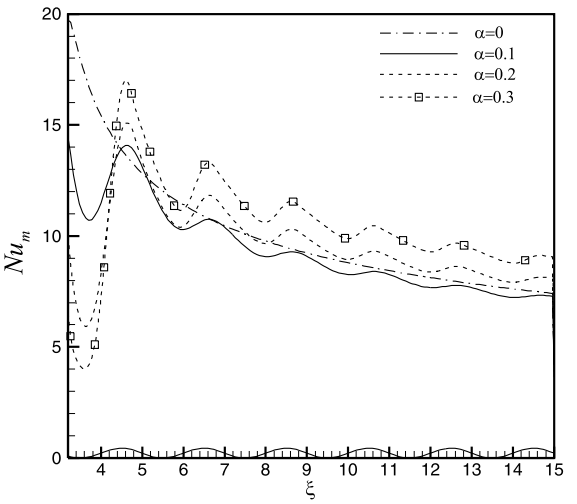

Fig. 6. Distribution of average Nusselt number for $Re = 500$ and $Pr = 6.93$.

flow reversal causes the harmonic curves of the skin-friction coefficient (show in Fig. 3) to become different to the wavy surface in each furrow of the wavy-wall channel. Thus, for a complete cycle (e.g. $4 < \xi < 6$), the maximum value is located at $\xi = 4.5$, which is the minimum cross-section of the wavy surface, but the minimum value is located at $\xi = 5.9$, which is not at the maximum section of the wavy surface ($\xi = 5.5$).

Fig. 5 shows that the local Nusselt number is higher in the converging section of each wave than in the diverging section (furrow). This is because the converging section has a higher average velocity and velocity gra-

dient, which increases the heat transfer ratio. Conversely, the flow reversal has a low velocity gradient near the wall surface in each furrow, which decreases the heat transfer ratio. Furthermore, the minimum local Nusselt number is located upstream within a short distance of the maximum section of each wave for $\alpha = 0.1$, and this distance increases as the wavy amplitude–wavelength ratio is increased to $\alpha = 0.2$. This is because as wavy amplitude–wavelength ratio is increased, the strength of the flow reversal also increases, and the separated point moves closer to the minimum section of the wavy-wall channel.

As shown in Eq. (28), the average Nusselt values may be obtained by averaging the heat transfer over a surface, which is based on the total area of each wave, and not on projected area, from the start point of the wavy surface to $\sigma(x)$. From the standpoint of the average Nusselt number as shown in Fig. 6, it appears that the highest average Nusselt numbers belongs to the first wave and that the Nusselt number stays uniform downstream of the third wavy as a result of the flow being periodically fully developed. The average Nusselt value for a small amplitude–wavelength ratio, i.e. $\alpha = 0.1$, does not increase too much than for a flat-wall channel. This is because the Nusselt number (see Fig. 5) in the diverging section of each wave makes only a relatively small contribution. However, higher wavy amplitude–wavelength ratios ($\alpha = 0.2$ and 0.3) result in higher average Nusselt numbers. This result may also be explained from Fig. 5. The amplitude of the Nusselt number increases with wavy amplitude–wavelength ratio, and the quantity of the Nusselt number will also increase. Both inferences are manifest in the converging section of the wavy-wall channel and in a tiny change in the diverging section.

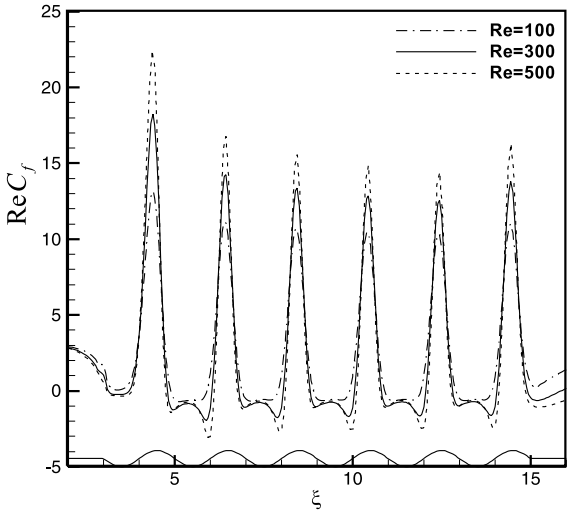

Fig. 7. Distribution of skin-friction coefficient for $\alpha = 0.2$ and $Pr = 6.93$.

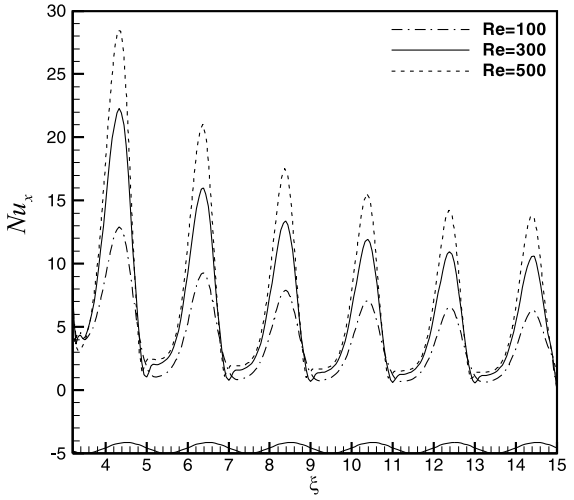

Fig. 8. Distribution of local Nusselt number for $\alpha = 0.2$ and $Pr = 6.93$.

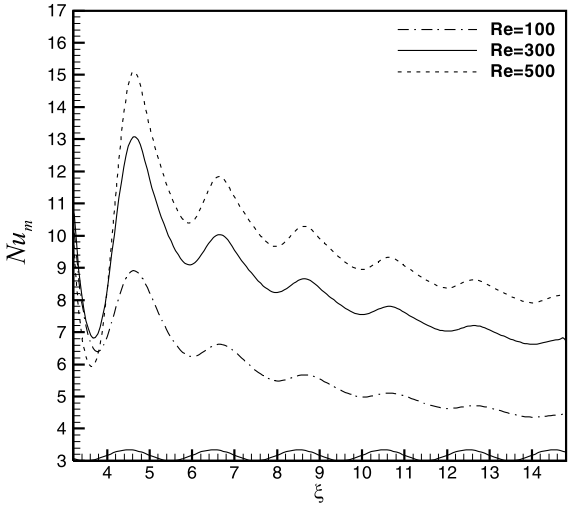

Fig. 9. Distribution of average Nusselt number for $\alpha = 0.2$ and $Pr = 6.93$.

Figs. 7–9 show the distribution of the local skin-friction coefficient, local Nusselt number and average Nusselt number for $Re = 100$, 300 and 500, $\alpha = 0.2$, and $Pr = 6.93$. Figs. 7 and 8 show that the skin-friction coefficient and Nusselt number distribution have the highest magnitude on the first wave, although the distributions of skin-friction and heat transfer follow the same pattern for all corrugations. As the Reynolds number increases, the amplitude of the skin-friction coefficient and the local Nusselt number will also in-

crease. It should be noted that as the Reynolds number is decreased from 500 to 100, the minimum skin-friction coefficient of each wave increases and approaches the zero. This indicates that the nonlinear convection terms are relatively small compared with the diffusion effects when the Reynolds number is less than 100. In addition, although the reticulation zones increase in size when the Reynolds number increases, the Nusselt number and the skin-friction coefficient decrease slightly in the furrow of each wave. Thus, with an increase in the Reynolds number, the maximum values of the friction coefficient and of the Nusselt number increase in each converging section, but their minimum values remain almost constant in the diverging section.

The distributions of average Nusselt number for various Reynolds numbers are plotted in Fig. 9. The maximum and minimum values of the average Nusselt number occur almost at the minimum and downstream maximum cross-sections of the wavy-wall channel. The first wave shows a higher average heat transfer coefficient. As the axial coordinate increases, the amplitude of the average Nusselt number decreases. This is to be expected since the average Nusselt number is obtained by integrating the local Nusselt number distribution over the area. The average Nusselt number is constant after the third wave, i.e. as soon as the flow becomes periodically fully developed. Also, a higher Reynolds number results in a higher average Nusselt number for all the waves.

Figs. 10 and 11 show the variations in average Nusselt number with Reynolds number for different amplitude wavelength ratios at $Pr = 6.93$ and 0.71, and include the limiting case of a flat surface ($\alpha = 0$) for comparison purposes. The enhancement of heat transfer with Reynolds number and wavy wall is clear. The average Nusselt numbers for the wavy-wall channel with a smaller amplitude wavelength ratio, such as $\alpha = 0.1$, are only slightly larger than those for a parallel-plate channel. With a larger amplitude wavelength ratio, such as $\alpha > 0.2$, there is again no significant heat transfer enhancement at low Reynolds numbers, but at a significantly higher Reynolds number, the corrugated channel is an effective heat transfer device. Additionally, this effect of heat transfer increases with increasing Prandtl number.

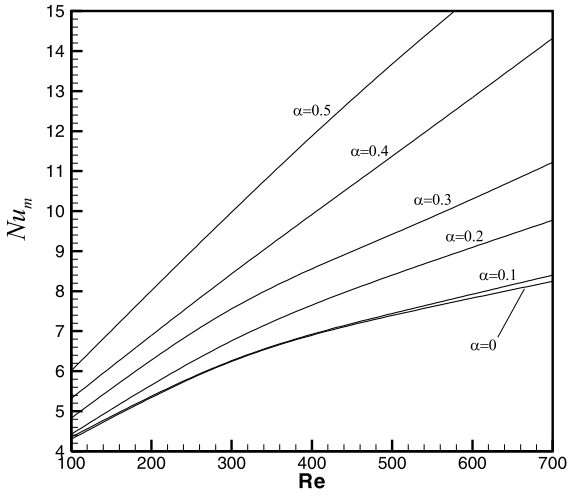

Fig. 10. Variation of Nusselt number with Reynolds number for different amplitude wavelength ratios at $Pr = 6.93$.

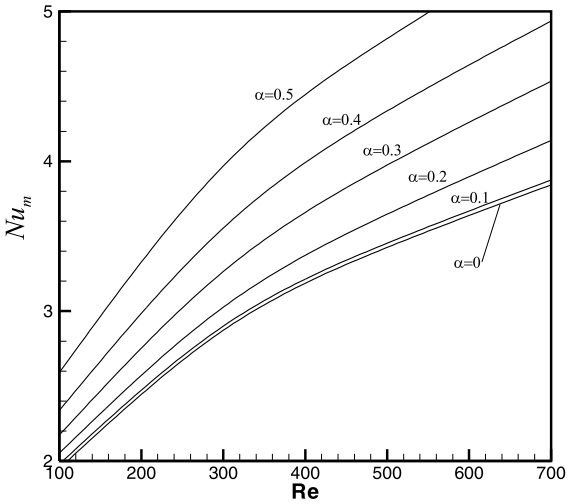

Fig. 11. Variation of Nusselt number with Reynolds number for different amplitude wavelength ratios at $Pr = 0.71$.

5. Conclusions

Forced convection for flow through a periodic array of a wavy-wall channel has been investigated numerically. A simple coordinate transformation method was employed to transform the complex wavy-wall channel into a parallel-plate channel. The spline alternating-direction implicit method was then used to solve the flow patterns and the heat transfer characteristics. Effects of the wavy geometry, Reynolds number and Prandtl number on the local skin-friction coefficients and Nusselt numbers were studied. Results show that the flow through a periodic array of a wavy-wall channel forms a highly complex flow pattern, which comprises a strong forward flow and an oppositely directed recirculating flow with each wave. The harmonic curves for the local skin-friction coefficient and the local Nusselt number have the same frequency as that of the wavy surface at smaller wavy amplitude–wavelength ratios or at lower Reynolds numbers. The major region of flow reversal occurs at higher Reynolds numbers, and causes the harmonic curves of the skin-friction coefficient and the Nusselt number to be different to the

wavy surface in the diverging section of each wave. In the converging section, the peaks of skin-friction coefficient and Nusselt number occur near the peak of the wavy wall and are independent of the amplitude–wavelength ratio and the Reynolds number. The minimum quantities of the skin-friction coefficient and of the Nusselt number are located downstream and upstream within a short distance of the maximum section of each wave. Moreover, this distance increases with increasing wavy amplitude–wavelength ratio and Reynolds number. However, as the wavy amplitude–wavelength ratio and the Reynolds number increase, the local Nusselt number increases manifestly in the converging section of the wavy-wall channel and shows a small change in the diverging section. Thus, at significantly larger amplitude wavelength ratios, the corrugated channel is an effective heat transfer device, especially for higher Reynolds numbers.

References

[1] J.C. Burns, T. Parks, J. Fluid Mech. 29 (1967) 405–416.
[2] J.L. Goldstein, E.M. Sparrow, ASME J. Heat Transfer 99 (1977) 187.
[3] J.E. O'Brien, E.M. Sparrow, ASME J. Heat Transfer 104 (1982) 410.
[4] N. Saniei, S. Dini, ASME J. Heat Transfer 115 (1993) 788.
[5] G. Wang, P. Vanka, Int. J. Heat Mass Transfer 38 (17) (1995) 3219.
[6] T.A. Rush, T.A. Newell, A.M. Jacobi, Int. J. Heat Mass Transfer 42 (1999) 1541.
[7] S. Blancher, R. Creff, P.L. Quere, Int. J. Heat Fluid Flow 19 (1998) 39.
[8] S. Selvarajan, E.G. Tulapurkara, V.V. Ram, A numerical study of flow through wavy-walled channels, Int. J. Numer. Meth. Fluids 26 (1998) 519–531.
[9] M. Greiner, R.F. Chen, R.A. Wirtz, ASME J. Heat Transfer 113 (1991) 498.
[10] R.A. Wirtz, F. Huang, M. Greiner, ASME J. Heat Transfer 121 (1999) 236.
[11] M.W. Collins, Proc. Inst. Mech. Eng. 189 (15) (1975) 129.
[12] P. Wang, R. Kahawita, Int. J. Comput. Math. 13 (1983) 271.
[13] C.K. Chen, C.C. Wang, J. Thermophys. Heat Transfer 14 (2000) 340.
[14] S.G. Rubin, R.A. Graves, Comput. Fluids 1 (1975) 1.